

Ultrasound Scatterer Density Classification Using Convolutional Neural Networks by Exploiting Patch Statistics

Ali K. Z. Tehrani, Mina Amiri, Ivan M. Rosado-Mendez,
Timothy J. Hall, and Hassan Rivaz[‡]

December 7, 2020

Abstract

Quantitative ultrasound (QUS) can reveal crucial information on tissue properties such as scatterer density. If the scatterer density per resolution cell is above or below 10, the tissue is considered as fully developed speckle (FDS) or low-density scatterers (LDS), respectively. Conventionally, the scatterer density has been classified using estimated statistical parameters of the amplitude of backscattered echoes. However, if the patch size is small, the estimation is not accurate. These parameters are also highly dependent on imaging settings. In this paper, we propose a convolutional neural network (CNN) architecture for QUS, and train it using simulation data. We further improve the network performance by utilizing patch statistics as additional input channels. We evaluate the network using simulation data, experimental phantoms and *in vivo* data. We also compare our proposed network with different classic and deep learning models, and demonstrate its superior perfor-

mance in classification of tissues with different scatterer density values. The results also show that the proposed network is able to work with different imaging parameters with no need for a reference phantom. This work demonstrates the potential of CNNs in classifying scatterer density in ultrasound images.

1 Introduction

Ultrasound imaging is increasingly attracting the attention of researchers and clinicians due to being a real-time and non-ionizing imaging modality, and being less expensive and more portable compared to other medical imaging techniques. However, several types of artifacts make interpretation of ultrasound images difficult. Cells, collagen, microcalcifications, and other microstructural components are often smaller than the wavelength of the ultrasound wave, and scatter the wave and create the granular appearance called speckles. The scattered signal from scatterers provides useful information about characteristics of the scatterers which are highly related to the tissue properties. Quantitative ultrasound (QUS) measures the tissue characteristics by analysing the ultrasound signal [1–6]. It aims to provide quantitative estimations of tissue characteristics which cannot be otherwise obtained from the B-mode image. It has been employed in many different applications such as liver fibrosis [7, 8], bone quality measurement [9], breast tumor classification [10, 11] and cardiac tissue characterization [12]. Improving QUS techniques can eventually broaden the applications of this safe and

*This work has been submitted to the IEEE for possible publication. Copyright may be transferred without notice, after which this version may no longer be accessible. This work is supported by the Natural Sciences and Engineering Research Council of Canada (NSERC) RGPIN-2020-04612.

[†]A. K. Z. Tehrani, M. Amiri and H. Rivaz are with the Department of Electrical and Computer Engineering, Concordia University, Canada. Ivan M. Rosado-Mendez is with Universidad Nacional Autonoma de Mexico, Mexico. Timothy J. Hall is with the Department of Medical Physics, University of Wisconsin, United States. e-mail: A_Kafaei@encs.concordia.ca, Amirim@encs.concordia.ca, irosado@fisica.unam.mx, tjhall@wisc.edu and hrivaz@ece.concordia.ca

[‡]Manuscript received; revised

cost-effective method in diagnosis and treatment of a large number of disorders.

QUS methods can be classified into two broad categories: spectral-based and envelope-based methods [13]. Parameters such as the backscatter coefficient and attenuation coefficient can be estimated by spectral-based methods, usually with a requirement of a reference phantom to remove system-dependent effects [5, 14, 15]. In envelope-based methods, different characteristics of the tissue is usually estimated by analysing and modeling the envelope of the ultrasound RadioFrequency (RF) data by fitting a probability density function. The sample size, wave frequency, and the attenuation can affect the accuracy of the distribution modeling, and therefore its parameter estimations [16, 17].

The statistics of echo-envelope data, extracted by either model-based or model-free parameters, provide information about tissue properties. Model-based parameters try to fit a distribution to the envelope data. If there are many scatterers (more than 10 in a resolution cell (an ellipsoidal volume defined by - 6 dB point of the beam profile [18])), the envelope data is considered as a fully developed speckle (FDS), and the RF data can be modeled by the Gaussian distribution; therefore, envelope values follow the Rayleigh distribution [1, 19, 20]. However, when the number of scatterers is low, the resolution cell has low-density scatterers (LDS); therefore, the Rayleigh distribution fails to model the envelope statistics. To model LDS, other distribution such as K-distribution [12], Homodyned K-distribution [21, 22] and Nakagami distribution [10] can be utilized. Among these, Homodyned K-distribution is the most comprehensive but the most complex that does not have a closed-form solution. The Nakagami distribution provides a good estimate of the envelope signal with low-complexity and is widely used in QUS studies.

The Nakagami image, originally proposed by [10], can be used to describe different probability density functions, and to characterize various scatterer patterns in tissues. It has been shown to be useful in discriminating different scatterer concentrations and tissue types. The Nakagami image can depict tissue properties that are not visible in ultrasound B-mode images, and has been employed in several studies for

tissue characterization [7, 23–25].

Model-free parameters such as the envelope signal to noise ratio (SNR), skewness (S) and entropy [20, 26] are statistical parameters that change with different scatterer distributions. Entropy parametric imaging is a QUS imaging technique, which uses a small sliding window throughout the image to measure the entropy (the overall level of variations) of the backscattered RF signal. It has been shown to be effective in differentiating tissues with different scattering properties, and can provide higher accuracy in a smaller patch size compared to Nakagami imaging [26].

Deep Learning (DL) techniques have been utilised in many fields of medical image processing. They have also proved useful in different ultrasound applications such as segmentation [27, 28], super resolution imaging [29–31] and elastography [32–34]. A few studies have also attempted to tackle the challenge of extracting quantitative measures from ultrasound images using DL techniques. Byra *et al.* [35] used Nakagami images to train a convolutional neural network for the task of breast lesion classification. Wang *et al.* [36] have proposed a 3D convolutional network for breast cancer detection. However, the appearance and even statistics of ultrasound images can change with changes in imaging parameters such as time gain compensation and focal points. Such changes are well studied in DL and are referred to as domain shift [37]. If not accounted for, domain shift renders DL estimates grossly inaccurate. In fact, this is one of the reasons that DL is less explored in QUS compared to other ultrasound applications.

In a recent work, we designed a CNN to classify FDS and LDS [38]. The CNN was fed with envelope data and the RF data spectrum from small patches of RF data, and was compared with a Multi-Layer Perceptron (MLP) classifier, which used SNR and skewness as inputs. We used patches to analyse a small area of the image and therefore, to provide a high resolution. The effect of patch size was also investigated (with patches sized 5 to 10 \times wavelength). The results showed that in small patch sizes, the CNN outperformed the MLP classifier, whereas for larger patch sizes, where the statistics of the patch could be reliably estimated, the MLP classifier outperformed

the CNN.

In another recent work, we segmented simulated images with three different scatterer densities using a U-Net [39]. We found that the network was able to segment precisely when the intensity difference between the inclusion and the background was high thus the network could associate the intensity to the scatterer density.

In [40], the mean scattering cross section which is another QUS parameter was estimated for the whole image. They assumed that all regions have FDS which is a limiting factor in real ultrasound images. In this study, we aim to classify FDS from LDS regions using CNNs in small patches (Note that the patch size is different for simulation, experimental and *in vivo* data) where classical statistical parameters commonly used in QUS studies cannot be estimated accurately. We use the ultrasound envelope data as the input to the network, since statistics such as SNR and Nakagami parameters are histogram-based, meaning that they ignore image texture. We hypothesize that the texture of the ultrasound envelope image contains crucial information which can be useful to determine the density of scatterers.

We use a large amount of simulated data to train the network, and test the network on simulated, phantom and *in vivo* data. We show the effect of domain shift [37] caused by changes in imaging parameters on the results and the feature space. We also demonstrate that using both texture information and patch statistics helps improve the robustness against imaging parameters. We validate our methods using experimental phantoms and *in vivo* data which have different imaging parameters compared to the data used for training the networks. We also show the effect of transfer learning for domain adaptation. Our contributions can be summarized as follows:

- A CNN architecture is proposed to analyse the ultrasound envelope data for tissue characterization.
- The network is further improved by exploiting patch statistics which provide additional information.
- Extensive ablation experiments are done to find

the best input for the network in simulation and experimental phantoms, and to improve the robustness against variations of imaging parameters.

- Transfer learning is investigated to evaluate the network’s performance when it is fine-tuned with images of the test domain.
- Different classifiers (support vector machine (SVM), random forest and MLP) are used to classify based on patch statistics.
- Experimental phantom and *in vivo* data are employed to validate our work in different imaging settings.

2 Methods

In this section, we first describe different datasets we analysed. We then present the scatterer density classification methods developed in this work, which include both classical (SVM, random forest and MLP) and DL methods (CNN and CNN with patch statistics as additional inputs), and provide intuitions for using different inputs.

2.1 Data

We employed 3 different datasets to investigate the performance of our proposed methods as outlined below.

2.1.1 Simulation data

We simulated 200 phantoms of size $30\text{ mm} \times 30\text{ mm} \times 1\text{ mm}$ using the Field II pro toolbox [41], with the center frequency of 6.67 MHz. The sampling frequency was 100 MHz and the RF signals were then down-sampled to 50 MHz. Other imaging parameters can be found in Supplementary Materials.

We randomly distributed point scatterers in the phantoms. In 100 FDS phantoms, we included 16 scatterers per resolution cell. In the remaining 100 LDS phantoms, we included 2 scatterers per resolution cell. The resolution cell size was determined by calculating the correlation between the data and

a moving window in different regions [42]. The size was 0.1 mm^2 at the focal point (The out of plane resolution cell size is not computed). We randomly cropped 5000 patches of size 256×32 ($4.04 \text{ mm} \times 5 \text{ mm}$ which is 17 and $21 \times$ wavelength in axial and lateral directions, respectively) from different depths as the training set and 1000 patches as the validation set. For the test set, we simulated 20 more phantoms with a random scatterer density value of 2 or $16 \pm 10\%$ in order to make the test data more challenging. We randomly selected 500 patches from these phantoms as the test set to evaluate the methods. This dataset will be publicly available online after acceptance of this paper at data.sonography.ai.

2.1.2 Experimental phantom

Three different phantoms were used to validate our method. The phantoms were of size $15\text{cm} \times 5\text{cm} \times 15\text{cm}$, built from homogeneous mixture of agarose gel media and glass beads as scattering agents. The glass bead diameter range and bead concentration in the phantoms are reported in Table 1. For more information on construction details, the speed of sound and attenuation coefficient of these phantoms refer to [43]. The phantoms were imaged using an 18L6 transducer operating at 10 MHz frequency using an Acuson S2000 scanner (Siemens Medical Solutions, Malvern, PA) and the RF data was acquired using Aixius Direct Ultrasound Research Interface [44]. We computed the resolution cell size using correlation method at different depths and it varied between 0.284 mm^3 (at the top where resolution was poor) and 0.036 mm^3 (at the focal point where resolution was the highest). This high variation of the resolution cell size can have an adverse effect on the classification, especially when this variation is not observed by the network during training. The numbers of scatterers per resolution cell for different depth are given in Table 1.

We used the experimental phantoms as the test data to evaluate the performance of different models optimized or trained on the simulation data (with or without fine-tuning the network). Phantom A (high concentration) belongs to the FDS class and Phantoms B (medium concentration) and C (low concen-

tration) belong to the LDS class.

2.1.3 In vivo data

We used breast ultrasound images recorded by a Siemens Sonoline Elegra System (Issaquah, WA) with the sampling frequency of 36 MHz and a lateral beam spacing of $200 \mu\text{m}$. I-Q echo data were recorded in a file on the imaging system when data acquisition was stopped (frozen on the imaging system) [44]. The I-Q data were converted to RF echo data offline using the known modulation frequency of the imaging system. More information about this dataset and the recording procedure is provided in [45].

2.2 Classical Statistical Parameters

Several parameters have been proposed in literature for estimating the scatterer density in ultrasound images. SNR and skewness are among the most important parameters proposed to classify different scatterer densities:

$$R = SNR = \frac{\overline{A^v}}{\sqrt{A^{2v} - (\overline{A^v})^2}}, \quad (1)$$

$$S = skewness = \frac{\overline{(A^v - \overline{A^v})^3}}{(\overline{A^{2v}} - (\overline{A^v})^2)^{1.5}}$$

where A is the envelope of RF data, v is the signal power and $\overline{(\dots)}$ denotes mean operation. While in [1], v smaller than 1 was suggested due to having higher dynamic range and lower estimation error, Prager *et al.* proposed 1.8 as the optimal value [46] in terms of the estimation error. We analysed both recommended values of 0.5 and 1.8, and obtained significantly better results on the validation set using the 0.5 value (Area Under Curve (AUC) of 0.894 vs. 0.876 when employing the MLP, and 0.802 vs. 0.794 when employing the SVM classifier). We, therefore, set v to 0.5 in this study.

When the patch size is big enough, the estimation error of R and S , and therefore the classification error based on these parameters is low. But

Table 1: Characteristics of the experimental phantoms and their scatterer concentration per resolution cell using 18L6 transducer (the range shows the minimum and maximum values derived from different depths).

Phantom	Diameter of Random Scatterers (μm)	Scatterers Concentration per mm^3	Scatterers Concentration per resolution cell
A (High)	5-40	236	8.50-67
B (Medium)	75-90	9	0.32-2.55
C (Low)	126-151	3	0.11-0.85

for small-size patches, the classification becomes difficult [1,38]. This is especially important in clinical applications where tissues are rarely homogeneous and a large patch may include different scattering properties [20,21].

Another parameter which has been proposed for scatterer density classification is entropy [26]:

$$Entropy = \sum_{n=1}^N p(i) \log[p(i)] \quad (2)$$

where statistical histogram of the envelope data square is represented by p , and N is the number of bins for calculating the histogram, which is arbitrarily set to 100 in this study. Entropy increases as the density of scatterers increases (moving from LDS to FDS). The entropy measure is shown to be effective when using a small window for QUS analysis [26].

Another parameter that has been shown useful in estimation of scatterer density is the Nakagami model parameters m (a maximum likelihood estimator of the shape parameter) and T (a generalized likelihood ratio test statistic) [19]:

$$m = \frac{(\overline{A^2})^2}{var[A^2]},$$

$$T = 2K \left(\log \frac{m^m}{\Gamma(m)} + (m-1) [\log(\overline{I}) - \log(\overline{I}) - 1] \right) \quad (3)$$

where A is the envelope data and Γ represents the Gamma function. I is a vector representing K independent and identically distributed samples of the intensity from a specific patch. Different values of m explain different properties; when the m parameter approaches 1, the distribution approaches the

Rayleigh distribution. The m parameter above and below 1 represent post- and pre-Rayleigh distributions, respectively, which are forms of a more general family of distributions, called Rician [1, 10, 18, 47].

There is a strong correlation between features m and T . The features m and R are also highly correlated. We therefore, remove the feature m from the feature list to eliminate the redundancy between different features. We consider aforementioned parameters as a set of features to classify FDS and LDS patches. The Supplementary Materials contain detailed correlation analysis of these statistical parameters.

Fig. 1 shows the distribution of different features, extracted from the simulation training data for LDS and FDS classes. The patch size is small so that for all features, a considerable overlap exists between the distributions of the two classes, which makes the classification highly erroneous using only a single feature. As opposed to our previous work [38] where only parameters R and S were used for classification, we use R , S , entropy and T together to obtain higher performance in classification. As shown in Fig. 1, the dynamic range of the features are not similar, hence we employ normalization (they are normalized to be in range 0-1) across each feature in the training data. The test and validation data were also normalized using the same coefficient obtained from the training data.

2.3 Machine Learning Methods

In order to classify FDS and LDS classes, we developed classical machine learning techniques in addition to DL methods. In this section, we describe the details of these classic techniques.

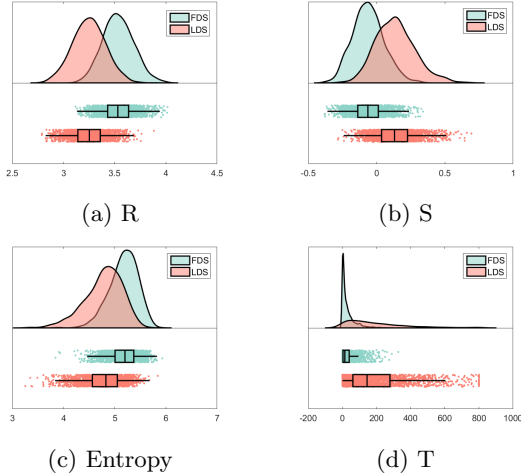


Figure 1: The distribution of the patch statistics for FDS and LDS in simulated training data. The patch size is small enough such that FDS and LDS classes overlap.

2.3.1 Support Vector Machine (SVM)

We used SVM as a classical machine learning algorithm to classify FDS versus LDS. We analysed different SVMs with linear and non-linear (Radial Basic Function (RBF) and polynomial) kernels. An SVM with an RBF kernel led to the best results on the validation set, and was selected throughout this manuscript.

2.3.2 Random forest classifier

Random forest is a learning method based on the decision tree algorithm and ensemble of different trees' outputs, and is amongst the top classification algorithms. By changing different parameters of a random forest model, we found the best performing model on the validation set, and used this model to classify different patches of simulation and experimental phantom data.

2.4 Deep Learning Methods

2.4.1 Multi-Layer Perceptron (MLP)

We proposed an MLP structure to classify FDS and LDS groups. To find the best network architecture for classifying scatterer density using the aforementioned features, we investigated the performance of different MLP architectures on the validation data. We obtained the best results with a 3-layer network. Further increase in the number of layers did not improve the results and lead to overfitting, a common problem with MLPs. We also analysed different numbers of neurons in each hidden layer. We incrementally increased the number of neurons in two hidden layers. Including 128 neurons in the first hidden layer, and 32 neurons in the second hidden layer led to the best result. However, it is important to note that the results reached a plateau and did not change substantially by changing the number of neurons. We employed Batch Normalization [48] in the first and second layers and Dropout [49] in the second layer. The activation functions were Tanh for the first two layers and Sigmoid for the last layer. The loss function was binary cross entropy and the network was optimized using the Adam optimizer.

2.4.2 Convolutional Neural Network (CNN)

We used a CNN to classify the scatterer density. Our proposed CNN structure is presented in Fig. 2. The input can have one or two channels. The FDS group was considered as the class with label 1, and the LDS group was considered as the class with label 0. The output of the network is the probability of being FDS. The network contains the following components:

- Residual blocks: Each residual block consists of 2 convolutional layers with a skip connection followed by another convolutional layer and an average pooling layer of size 2×2 . Using residual blocks provides the ability to train deeper and therefore more efficient networks by eliminating the vanishing gradient issue which happens in deep networks [50].
- Convolution block: The network consists of two convolutional blocks before and after the residual

blocks to extract features.

- Fully-connected layers: Two fully connected layers are used in the final step for classification. The first fully connected layer employs Dropout for regularization.

2.4.3 CNN with patch statistics as additional inputs

To further enhance the network, we propose to utilize the patch statistics (R , S , entropy and T) as additional inputs. We tested different settings to determine the optimal way to fuse the information of patch statistics to the CNN. Fig. 2 shows the outcome (A denotes envelope). The CNN part is the same as the CNN network described in section D-2 and the patch statistic classifier part is similar to the MLP explained in section D-1. These parameters are fed to an MLP to generate a feature map, which is concatenated to the feature map obtained from the CNN. The resulted feature map is then used for a final classification.

Our first intuition was to train the whole network end to end. However, the CNN and the MLP have vastly different numbers of parameters and this resulted in a low generalization and a large sensitivity to the initial seeds. To mitigate the imbalanced number of parameters, we proposed training each part separately. We then trained the fusing part while the CNN and MLP weights were kept fixed. Please refer to the Supplementary Materials for more information regarding the training strategy.

2.5 Training Schedule

To augment the data, random Gaussian noise, elastic deformation and random flipping in lateral direction were employed. The networks were trained with the Adam optimizer and the binary cross entropy was used as the loss function. Due to the fact that there were different networks with different inputs and to have a good generalization, we adopted a variant of early stopping which could be considered as a form of implicit regularization [51]. For early stopping, the validation AUC was selected as the stopping criteria;

when the best validation AUC was reached during the training and remained the best after 20 epochs, we stopped the training. The cyclic learning rate was also used in order to avoid bad local minima [52].

2.6 Input Channels

In [22], log compression of envelope along with the envelope have been used ($\log(A)$ and $A^2 \times \log(A^2)$) for estimating statistics using the Homodyned K-distribution. Inspired by their work, we used $A \times \log(A)$ as a novel input to the proposed CNNs. We therefore investigated different types of inputs for our proposed network architectures, including the amplitude alone A , $A \times \log(A)$, and both A and $A \times \log(A)$ as two different channels (Fig. 2). We also tested other inputs including $\log(A)$ and \sqrt{A} but did not observe any improvements. For brevity, the results are not included in the manuscript.

2.7 Transfer Learning

To evaluate the performance of our proposed networks on the experimental phantom data and *in vivo* data, we performed transfer learning for the top performing model using 8 frames of phantoms A and B. The frames' location was far from the test frames to avoid data leakage. We randomly cropped 1000 patches and fine-tuned CNN and MLP separately. Similar to the training, we used cycling learning but with smaller learning rate since only small changes were required for the network adaptation.

2.8 Evaluation Metrics

To evaluate the classification performance, we used AUC of the Receiver Operating characteristic Curve (ROC) and also Youden's Index [53]. We estimated the 95% confidence interval of AUC by employing boot strapping (i.e. sampling the data with replacement, for 1000 times). Youden's Index is a measure of both sensitivity and specificity:

$$\begin{aligned}
 J &= \frac{TP}{TP + FN} + \frac{TN}{TN + FP} - 1 \\
 &= \textit{Sensitivity} + \textit{Specificity} - 1
 \end{aligned}
 \tag{4}$$

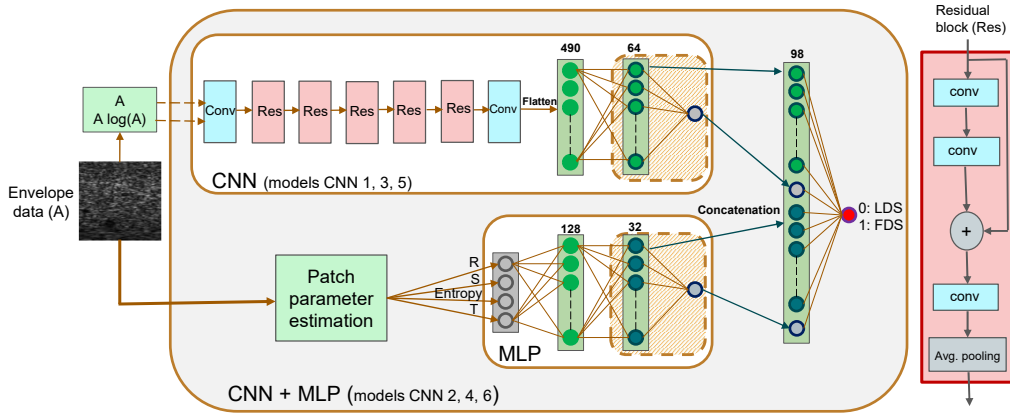


Figure 2: Proposed architecture for different networks.

Table 2: Results of different classification models on simulation data.

Model	Input	Patch Statistics	AUC (%)	Youdens' Index
SVM	A	✓	0.892 (0.867- 0.920)	0.62
Random forest	A	✓	0.894 (0.868- 0.919)	0.62
MLP	A	✓	0.894 (0.874- 0.912)	0.61
CNN 1	A	✗	0.957 (0.942- 0.966)	0.79
CNN 2	A	✓	0.957 (0.944- 0.967)	0.80
CNN 3	$A \times \log(A)$	✗	0.907 (0.887- 0.925)	0.67
CNN 4	$A \times \log(A)$	✓	0.924 (0.904- 0.939)	0.71
CNN 5	$A, A \times \log(A)$	✗	0.963 (0.949- 0.973)	0.82
CNN 6	$A, A \times \log(A)$	✓	0.964 (0.952-0.973)	0.82

where TP , FN , TN and FP denote true positive, false negative, true negative and false positive, respectively. We calculated the Youden’s Index for different threshold values and the highest values are compared between different models.

3 Results

In this section, we provide the results of the proposed models for classification of FDS and LDS classes when analyzing different datasets. We tested three classifiers without including any CNN (i.e. a SVM, a random forest and an MLP model). Different CNNs were also analysed, by including (CNNs 2,4,6) or excluding the MLP branch (CNNs 1,3,5), and by considering different inputs to the network including the envelope alone (CNNs 1,2), the envelope multiplied by the log compressed envelope (CNNs 3,4), and both images as two separate channels (CNNs 5,6-Fig. 2). All DL models were trained according to the training schedule explained in Section II-E. The weights of the top-performing network will be publicly available online after acceptance of this paper at data.sonography.ai.

3.1 Simulation Results

All proposed models were evaluated on the simulation data. The AUC values and Youden’s indexes are represented in Table 2, and the ROC curves of different methods are shown in Fig. 3. As seen in Table 2, CNN-based models provide better results compared to the MLP and SVM and random forest models. CNN 6 achieves the best AUC (0.964) among all studied models.

According to the results, exploiting the patch statistics is helpful (compare CNN 1 vs. 2, 3 vs. 4 and 5 vs. 6). It shows that classical patch statistic parameters provide complementary information to the CNN. Interestingly, the envelope (A) gives better results compared to ($A \times \log(A)$). However, using both inputs as two separate channels provides the best results (compare CNNs 1, 3 and 5).

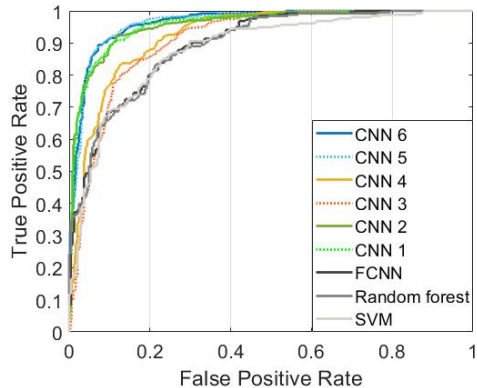


Figure 3: ROC curves of different models on simulation test data.

3.2 Experimental Phantom Results

The results of classifying small patches from phantom A vs. phantoms B and C are provided in Table 3, and the ROC curves are shown in Fig. 4. The patch size in terms of number of pixels is the same as the simulation data but it differs in terms of size in mm ($4.92 \text{ mm} \times 4.28 \text{ mm}$). Similar to the results on the simulation data, utilizing the patch statistics (CNNs 5 and 6) boosts the results (Table 3 and Fig. 4).

By comparing the results of simulation and experimental phantoms, we observe that the models with the envelope input (CNNs 1 and 2) perform well for the simulation data but poorly for the experimental data (compare Fig. 3 and Fig. 4). The models with both inputs (CNNs 5 and 6) have the best results for both simulation and experimental phantom data. CNN 6 has the best result among all models without fine-tuning (AUC=0.955 and Youden’s Index=0.79).

With only using the simulation data for training, we can still classify the experimental phantoms although the changes in imaging parameters and real artifacts in the experimental phantom data make the classification more challenging. However, employing both patch statistics and texture information extracted by CNNs using the proposed inputs (A and $A \times \log(A)$) improves the robustness of the network.

Fig. 5 depicts some examples of the studied images using different models. We split each image into over-

lapping patches (50% overlap), and feed all patches to the network. As seen in Fig. 5, CNNs 5 and 6 perform very well in classification of patches from phantoms A and C but they estimate high probability of being FDS for patches from phantom B which is not the correct class. However, according to the Table 3, these two networks have very high AUCs (0.949 and 0.955). These apparent contradictory results can be explained by the fact that AUC is not sensitive to threshold values and by considering a high threshold for classification, phantom A can be discriminated from phantoms B and C. Because of the domain shift from the simulation to experimental data, the networks trained on the simulation data predict high probability of being FDS for the phantom B. Interestingly, the opposite effect is observed for the MLP which uses only patch statistics; The MLP results in low score values for all three phantoms which is in contrast to CNN 5. Combining both CNN and MLP (CNN 6) leads to an improvement. To tackle the domain shift problem, CNN 6 is fine-tuned with images of the experimental phantom domain. The fine-tuned network correctly predicts low probability of FDS for most of patches in the phantom B in contrast to the CNNs trained only on the simulation data. Please refer to the Supplementary Materials for further details.

We should also mention that the networks estimate higher probability of FDS in the top and bottom regions of the phantoms. The main reason is that in these regions, the resolution cell size is larger than focal region, leading to a larger number of scatterers per resolution cell.

To have a better intuition of the trained CNNs, we visualize the feature maps of CNN 5 and CNN 6 before the last layer using the t-SNE method [54]. The feature maps are vectors of length 98 for CNN 6 and 64 for CNN 5. By the t-SNE method we reduce the dimension to be able to visualize them in 2D. Figure 6 shows the t-SNE representation of features extracted by the CNN part of the network (Fig. 6A), and by the whole network (model CNN 6- Fig. 6B). It is clear that combining the CNN and MLP networks has led to a better separability of the two classes of LDS and FDS.

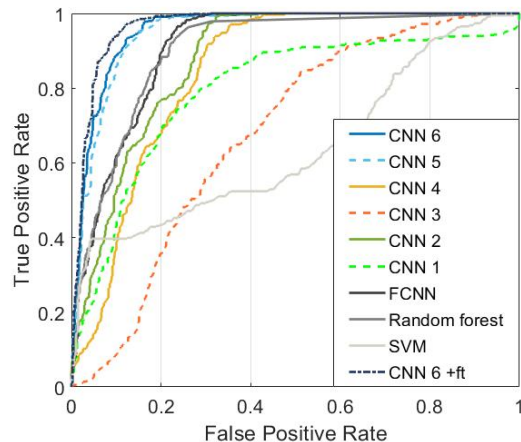


Figure 4: ROC curves of experimental phantoms. There is a considerable difference between single channel CNNs with/without utilizing patch statistics. CNN 5 and CNN 6 which use $A \times \log(A)$ and A as input channels perform well for experimental data. Fine-tuning further improve CNN 6 by removing domain shift.

3.3 *In vivo* Results

We evaluated our proposed method using *in vivo* data from three different patients. Fig. 7 demonstrates the results of model CNN 6 + ft on the *in vivo* data. The actual number of scatterers in different regions of the image is unknown. However, we expect the fat tissue in breast to be classified mostly as the FDS class, and regions with specular reflections not as FDS [55].

The patch size is $2.55 \text{ mm} \times 2.36 \text{ mm}$ which is small to have high spatial resolution. To gain a better resolution, we considered an overlap of 87.5% between patches when analysing the *in vivo* data. As seen in the figure, the areas with specular reflections with large or aligned scatterers are detected as the LDS group, as expected and regions with relatively homogeneous speckle are classified as regions with fully developed speckle.

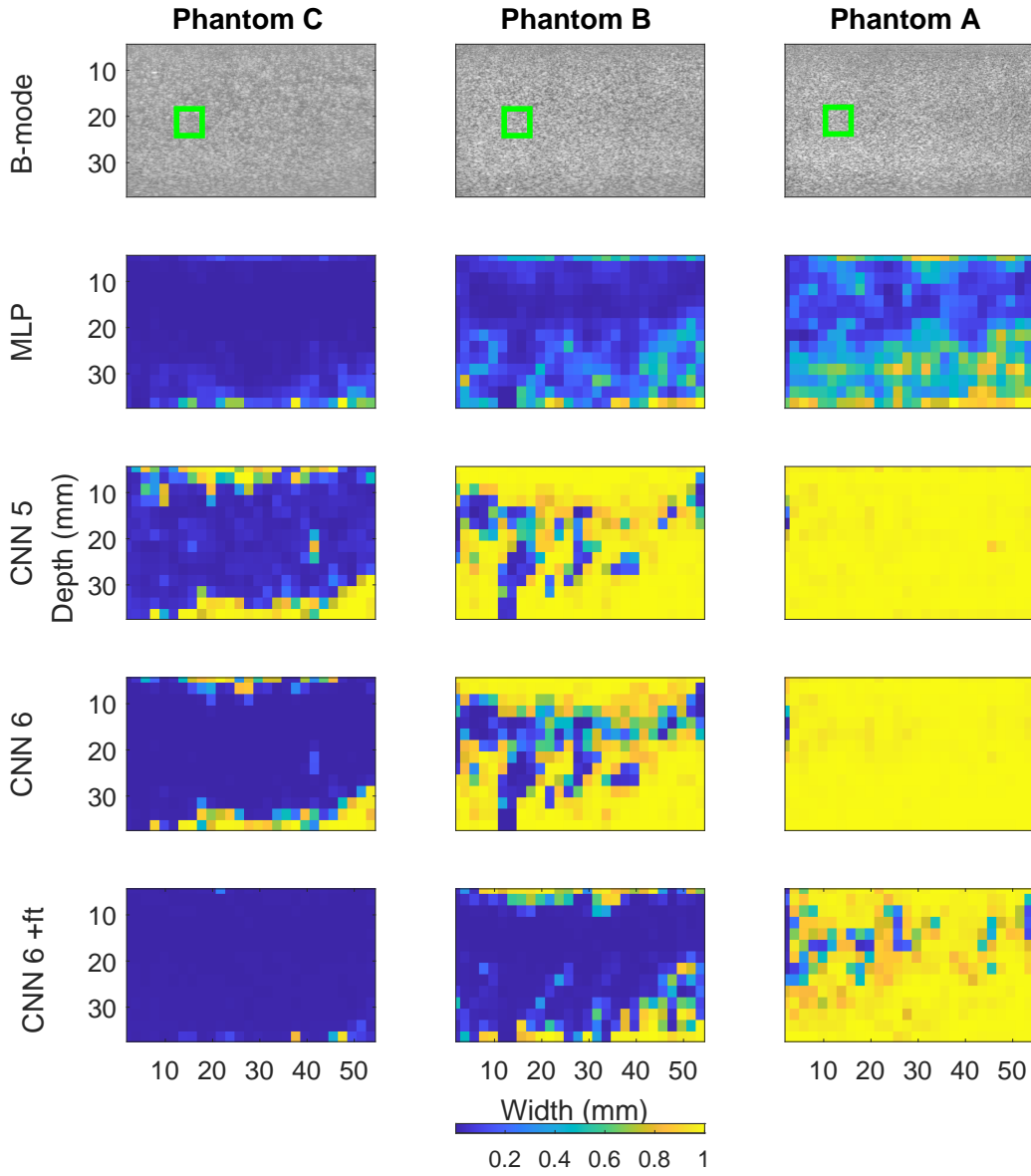


Figure 5: The results of MLP, CNN 5, CNN 6 and CNN 6 + ft models on the experimental phantoms. The color code represents the predicted output of the networks, from 0 (LDS) to 1 (FDS).

Table 3: Results of different classification models on experimental phantom data.

Model	Input	Patch Statistics	AUC (%)	Youdens' Index
SVM	A	✓	0.646 (0.623- 0.669)	0.35
Random forest	A	✓	0.895 (0.880- 0.913)	0.71
MLP	A	✓	0.894 (0.874-0.912)	0.72
CNN 1	A	✗	0.791 (0.781-0.802)	0.51
CNN 2	A	✓	0.877 (0.870-0.884)	0.66
CNN 3	$A \times \log(A)$	✗	0.679 (0.668-0.690)	0.31
CNN 4	$A \times \log(A)$	✓	0.845 (0.837-0.853)	0.49
CNN 5	$A, A \times \log(A)$	✗	0.949 (0.945-0.953)	0.79
CNN 6	$A, A \times \log(A)$	✓	0.955 (0.951-0.959)	0.79
CNN 6 + ft	$A, A \times \log(A)$	✓	0.966 (0.962-0.969)	0.85

4 Discussion

The density of scatterers in different parts of a tissue is an important property of that tissue which may discriminate normal and abnormal regions. Ultrasound images can be utilized to estimate this property non-invasively. This will eventually guide invasive procedures such as biopsy, leading to less expensive and safer diagnosis methods for different types of diseases. In this work, we employed DL techniques to classify the scatterer density in ultrasound images. Based on our results, different numbers of scatterers result in different texture patterns in the ultrasound image which can be detected by CNNs. Further investigations may reveal CNNs' effectiveness for other QUS problems.

The network trained on simulation data was able to classify the experimental phantom data, despite the fact that the number of scatterers and the imaging properties are completely different in these two datasets. Although transfer learning was not the main goal of this paper, we showed that it can help the network mitigate the domain shift problem. The impact of fine-tuning can be observed in phantom B which was challenging for the networks trained on the simulation data.

In a fixed imaging setting, a larger number of scatterers results in a brighter ultrasound image. However, by changing the imaging machine settings, the image intensity can vary. Even though the average density of ultrasound images contains information

about the scatterers concentration, it is not a reliable feature for classifying the number of scatterers, as it can be easily altered by changing the imaging setting. We eliminated the effect of the average intensity by normalizing each individual patch such that the intensity of all studied patches was in the range $[0,1]$.

The effective number of scatterers per resolution cell varies by depth and by the operating frequency. Generally, at the focal point, the resolution cell is the smallest. Therefore, there are fewer scatterers per resolution cell at the focal point compared to other regions. According to our experiments, there are more variations in real ultrasound data compared to the simulation data. One reason is that in simulation, we put the phantom with some distance to the probe, while in real ultrasound images, the entire image is obtained. Regarding the operating frequency, the small cells which are smaller than the wavelength are considered as scatterers. Therefore, the number of scatterers changes by the operating frequency (assuming the resolution cell size is fixed). In a tissue with cells in different sizes, lower center frequencies see more scatterers per resolution cell compared to the higher ones. The dependency of scatterer density on depth and frequency warrants further investigation.

We included the data recorded from three phantoms in this study. The density of the scatterers is not the only parameter which differs between these phantoms. The size of the included scatterers is also

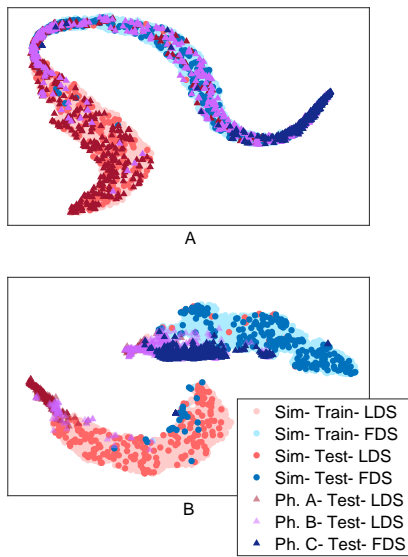


Figure 6: t-SNE visualization of the feature maps. (a) CNN without using patch statistics (CNN 5). (b) CNN with exploiting patch statistics (CNN 6). The feature map of CNN 6 is more separable than CNN 5. Sim: simulation data, Ph.: experimental phantom.

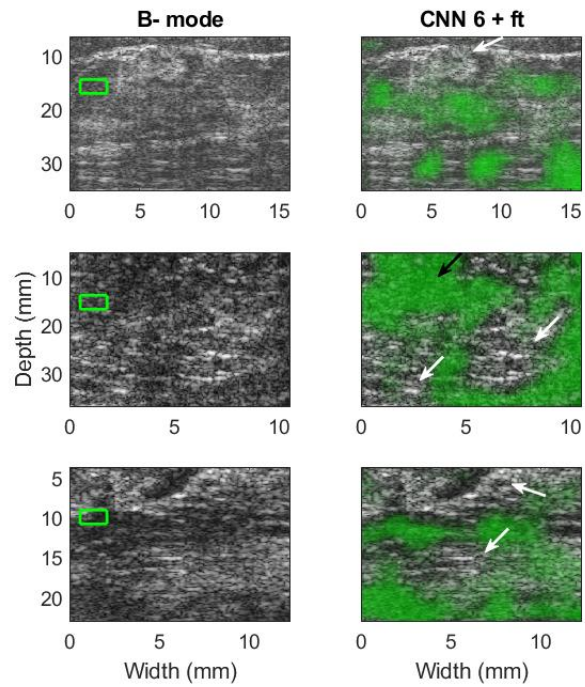


Figure 7: The results of CNN 6 + ft model on breast data from three different patients. The green overlaid color represents the areas detected as the FDS group. White arrows pinpoint the specular reflections in the ultrasound data. Black arrow shows the tissue region which looks like an FDS region in the B-mode image, as predicted by the network.

different (Table 1). However, considering the operating frequency, the size of the scatterers is still smaller than the wavelength, and does not substantially affect the results.

In this study, we were able to classify scatterer density in simulation and experimental phantoms. We also classified regions of homogeneous speckles as having FDS in the *in-vivo* data. This information can subsequently be used to detect different types of tissue abnormalities such as tumors and cancer tissues. This study therefore provides a fundamental tool for proceeding studies on tissue characterization.

5 Conclusion

In this manuscript, we proposed different CNN models to classify small patches of ultrasound images as FDS or LDS. We proposed to use both envelope and envelope multiplied by log compressed envelope as two separate input channels to the proposed CNNs. We also benefited from patch statistics by using an MLP along with the CNN to capture information of both texture and patch statistics. We finally validated our proposed method by experimental phantoms and *in vivo* data.

References

- [1] V. Dutt and J. F. Greenleaf, "Speckle analysis using signal to noise ratios based on fractional order moments," *Ultrasonic Imaging*, vol. 17, pp. 251 – 268, 1995.
- [2] K. Nam, J. A. Zagzebski, and T. J. Hall, "Simultaneous backscatter and attenuation estimation using a least squares method with constraints," *Ultrasound in Medicine and Biology*, vol. 37, no. 12, pp. 2096 – 2104, 2011.
- [3] M. F. Insana, R. F. Wagner, D. G. Brown, and T. J. Hall, "Describing small-scale structure in random media using pulse-echo ultrasound," *The Journal of the Acoustical Society of America*, vol. 87, no. 1, pp. 179–192, 1990.
- [4] J. Mamou and M. L. Oelze, *Quantitative ultrasound in soft tissues*. Springer, 2013.
- [5] Z. Vajihi, I. M. Rosado-Mendez, T. J. Hall, and H. Rivaz, "Low variance estimation of backscatter quantitative ultrasound parameters using dynamic programming," *IEEE Transactions on Ultrasonics, Ferroelectrics, and Frequency Control*, vol. 65, no. 11, pp. 2042–2053, 2018.
- [6] J. Rouyer, T. Cueva, T. Yamamoto, A. Portal, and R. J. Lavarello, "In vivo estimation of attenuation and backscatter coefficients from human thyroids," *IEEE transactions on ultrasonics, ferroelectrics, and frequency control*, vol. 63, no. 9, pp. 1253–1261, 2016.
- [7] M.-C. Ho *et al.*, "Using ultrasound nakagami imaging to assess liver fibrosis in rats," *Ultrasonics*, vol. 52, no. 2, pp. 215–222, 2012.
- [8] A. M. Pirmoazen, A. Khurana, A. El Kaffas, and A. Kamaya, "Quantitative ultrasound approaches for diagnosis and monitoring hepatic steatosis in nonalcoholic fatty liver disease," *Theranostics*, vol. 10, no. 9, p. 4277, 2020.
- [9] K.-Y. Chin and S. Ima-Nirwana, "Calcaneal quantitative ultrasound as a determinant of bone health status: what properties of bone does it reflect?," *International journal of medical sciences*, vol. 10, no. 12, p. 1778, 2013.
- [10] P. M. Shankar *et al.*, "Classification of ultrasonic b-mode images of breast masses using nakagami distribution," *IEEE Transactions on Ultrasonics, Ferroelectrics, and Frequency Control*, vol. 48, no. 2, pp. 569–580, 2001.
- [11] A. Larrue and J. A. Noble, "Modeling of errors in nakagami imaging: Illustration on breast mass characterization," *Ultrasound in Medicine and Biology*, vol. 40, no. 5, pp. 917 – 930, 2014.
- [12] L. Clifford, P. Fitzgerald, and D. James, "Non-rayleigh first-order statistics of ultrasonic backscatter from normal myocardium," *Ultrasound in Medicine and Biology*, vol. 19, no. 6, pp. 487 – 495, 1993.

- [13] M. L. Oelze and J. Mamou, "Review of quantitative ultrasound: Envelope statistics and backscatter coefficient imaging and contributions to diagnostic ultrasound," *IEEE Transactions on Ultrasonics, Ferroelectrics, and Frequency Control*, vol. 63, no. 2, pp. 336–351, 2016.
- [14] L. X. Yao, J. A. Zagzebski, and E. L. Madsen, "Backscatter coefficient measurements using a reference phantom to extract depth-dependent instrumentation factors," *Ultrasonic imaging*, vol. 12, no. 1, pp. 58–70, 1990.
- [15] F. Deeba *et al.*, "A spatially weighted regularization method for attenuation coefficient estimation," in *2019 IEEE International Ultrasonics Symposium (IUS)*, pp. 2023–2026, IEEE, 2019.
- [16] G. Cloutier, M. Daronat, D. Savéry, D. Garcia, L.-G. Durand, and F. S. Foster, "Non-gaussian statistics and temporal variations of the ultrasound signal backscattered by blood at frequencies between 10 and 58 mhz," *The Journal of the Acoustical Society of America*, vol. 116, no. 1, pp. 566–577, 2004.
- [17] P.-H. Tsui, Z. Zhou, Y.-H. Lin, C.-M. Hung, S.-J. Chung, and Y.-L. Wan, "Effect of ultrasound frequency on the nakagami statistics of human liver tissues," *PloS one*, vol. 12, no. 8, 2017.
- [18] R. F. Wagner, "Statistics of speckle in ultrasound b-scans," *IEEE Trans. Sonics & Ultrason.*, vol. 30, no. 3, pp. 156–163, 1983.
- [19] I. M. Rosado-Mendez, L. C. Drehfal, J. A. Zagzebski, and T. J. Hall, "Analysis of coherent and diffuse scattering using a reference phantom," *IEEE Transactions on Ultrasonics, Ferroelectrics, and Frequency Control*, vol. 63, no. 9, pp. 1306–1320, 2016.
- [20] H. Rivaz, E. M. Boctor, and G. Fichtinger, "Ultrasound speckle detection using low order moments," in *2006 IEEE Ultrasonics Symposium*, pp. 2092–2095, Oct 2006.
- [21] R. W. Prager, A. H. Gee, G. M. Treece, and L. H. Berman, "Analysis of speckle in ultrasound images using fractional order statistics and the homodyned k-distribution," *Ultrasonics*, vol. 40, no. 1-8, pp. 133–137, 2002.
- [22] F. Destrepes, J. Porée, and G. Cloutier, "Estimation method of the homodyned k-distribution based on the mean intensity and two log-moments," *SIAM journal on imaging sciences*, vol. 6, no. 3, pp. 1499–1530, 2013.
- [23] P.-H. Tsui, C.-K. Yeh, C.-C. Chang, and Y.-Y. Liao, "Classification of breast masses by ultrasonic nakagami imaging: a feasibility study," *Physics in Medicine & Biology*, vol. 53, no. 21, p. 6027, 2008.
- [24] P.-H. Tsui, C.-K. Yeh, C.-C. Chang, and W.-S. Chen, "Performance evaluation of ultrasonic nakagami image in tissue characterization," *Ultrasonic imaging*, vol. 30, no. 2, pp. 78–94, 2008.
- [25] P.-H. Tsui, C.-C. Huang, L. Sun, S. H. Dailey, and K. K. Shung, "Characterization of lamina propria and vocal muscle in human vocal fold tissue by ultrasound nakagami imaging," *Medical physics*, vol. 38, no. 4, pp. 2019–2026, 2011.
- [26] P.-H. Tsui *et al.*, "Small-window parametric imaging based on information entropy for ultrasound tissue characterization," *Scientific Reports*, vol. 7, no. 41004, 2017.
- [27] M. Amiri, R. Brooks, B. Behboodi, and H. Rivaz, "Two-stage ultrasound image segmentation using u-net and test time augmentation," *International journal of computer assisted radiology and surgery*, 2020.
- [28] K. M. Meiburger, U. R. Acharya, and F. Molinari, "Automated localization and segmentation techniques for b-mode ultrasound images: A review," *Computers in biology and medicine*, vol. 92, pp. 210–235, 2018.
- [29] R. J. Van Sloun, O. Solomon, M. Bruce, Z. Z. Khaing, Y. C. Eldar, and M. Misch, "Deep learning for super-resolution vascular ultrasound

- imaging,” in *ICASSP 2019-2019 IEEE International Conference on Acoustics, Speech and Signal Processing (ICASSP)*, pp. 1055–1059, IEEE, 2019.
- [30] K. G. Brown, D. Ghosh, and K. Hoyt, “Deep learning of spatiotemporal filtering for fast super-resolution ultrasound imaging,” *IEEE Transactions on Ultrasonics, Ferroelectrics, and Frequency Control*, 2020.
- [31] S. Goudarzi, A. Asif, and H. Rivaz, “Multi-focus ultrasound imaging using generative adversarial networks,” in *2019 IEEE 16th International Symposium on Biomedical Imaging (ISBI 2019)*, pp. 1118–1121, 2019.
- [32] Z. Gao *et al.*, “Learning the implicit strain reconstruction in ultrasound elastography using privileged information,” *Medical image analysis*, vol. 58, p. 101534, 2019.
- [33] E. Evain, K. Faraz, T. Grenier, D. Garcia, M. De Craene, and O. Bernard, “A pilot study on convolutional neural networks for motion estimation from ultrasound images,” *IEEE Transactions on Ultrasonics, Ferroelectrics, and Frequency Control*, 2020.
- [34] A. K. Z. Tehrani and H. Rivaz, “Displacement estimation in ultrasound elastography using pyramidal convolutional neural network,” *IEEE Transactions on Ultrasonics, Ferroelectrics, and Frequency Control*, pp. 1–1, 2020.
- [35] M. Byra, H. Piotrkowska-Wróblewska, K. Dobruch-Sobczak, and A. Nowicki, “Combining nakagami imaging and convolutional neural network for breast lesion classification,” in *2017 IEEE International Ultrasonics Symposium (IUS)*, pp. 1–4, 2017.
- [36] Y. Wang *et al.*, “Deeply-supervised networks with threshold loss for cancer detection in automated breast ultrasound,” *IEEE Transactions on Medical Imaging*, vol. 39, no. 4, pp. 866–876, 2020.
- [37] K. Stacke, G. Eilertsen, J. Unger, and C. Lundström, “A closer look at domain shift for deep learning in histopathology,” *arXiv preprint arXiv:1909.11575*, 2019.
- [38] A. K. Tehrani, M. Amiri, I. M. Rosado-Mendez, T. J. Hall, and H. Rivaz, “A pilot study on scatterer density classification of ultrasound images using deep neural networks,” in *2020 42nd Annual International Conference of the IEEE Engineering in Medicine & Biology Society (EMBC)*, pp. 2059–2062, IEEE, 2020.
- [39] M. Amiri, A. K. Tehrani, and H. Rivaz, “Segmentation of ultrasound images based on scatterer density using u-net,” in *2020 42nd Annual International Conference of the IEEE Engineering in Medicine & Biology Society (EMBC)*, pp. 2063–2066, IEEE, 2020.
- [40] L. Zhang, V. Vishnevskiy, and O. Goksel, “Deep network for scatterer distribution estimation for ultrasound image simulation,” *IEEE Transactions on Ultrasonics, Ferroelectrics, and Frequency Control*, 2020.
- [41] J. A. Jensen, “Field: A program for simulating ultrasound systems,” in *10th Nordicbaltic Conference On Biomedical Imaging, VOL. 4, Supplement 1, PART 1: 351–353*, Citeseer, 1996.
- [42] H. Rivaz, R. Zellars, G. Hager, G. Fichtinger, and E. Boctor, “9c-1 beam steering approach for speckle characterization and out-of-plane motion estimation in real tissue,” in *2007 IEEE Ultrasonics Symposium Proceedings*, pp. 781–784, IEEE, 2007.
- [43] I. M. Rosado-Mendez, *Advanced spectral analysis methods for quantification of coherent ultrasound scattering: Applications in the breast*. PhD thesis, The University of Wisconsin-Madison, 2014.
- [44] S. S. Brunke, M. F. Insana, J. J. Dahl, C. Hansen, M. Ashfaq, and H. Ermert, “An ultrasound research interface for a clinical system,” *IEEE transactions on ultrasonics, ferro-*

- electrics, and frequency control*, vol. 54, no. 1, pp. 198–210, 2007.
- [45] Y. Zhu and T. J. Hall, “A modified block matching method for real-time freehand strain imaging,” *Ultrasonic imaging*, vol. 24, no. 3, pp. 161–176, 2002.
- [46] R. Prager, A. Gee, G. Treece, and L. Berman, “Speckle detection in ultrasound images using first order statistics,” *University of Cambridge, Department of Engineering*, 2001.
- [47] T. Tuthill, R. Sperry, and K. Parker, “Deviations from rayleigh statistics in ultrasonic speckle,” *Ultrasonic imaging*, vol. 10, no. 2, pp. 81–89, 1988.
- [48] S. Ioffe and C. Szegedy, “Batch normalization: Accelerating deep network training by reducing internal covariate shift,” *arXiv preprint arXiv:1502.03167*, 2015.
- [49] N. Srivastava, G. Hinton, A. Krizhevsky, I. Sutskever, and R. Salakhutdinov, “Dropout: a simple way to prevent neural networks from overfitting,” *The journal of machine learning research*, vol. 15, no. 1, pp. 1929–1958, 2014.
- [50] K. He, X. Zhang, S. Ren, and J. Sun, “Deep residual learning for image recognition,” in *Proceedings of the IEEE conference on computer vision and pattern recognition*, pp. 770–778, 2016.
- [51] C. Zhang, S. Bengio, M. Hardt, B. Recht, and O. Vinyals, “Understanding deep learning requires rethinking generalization,” *arXiv preprint arXiv:1611.03530*, 2016.
- [52] L. N. Smith, “Cyclical learning rates for training neural networks,” in *2017 IEEE Winter Conference on Applications of Computer Vision (WACV)*, pp. 464–472, IEEE, 2017.
- [53] W. J. Youden, “Index for rating diagnostic tests,” *Cancer*, vol. 3, no. 1, pp. 32–35, 1950.
- [54] L. v. d. Maaten and G. Hinton, “Visualizing data using t-sne,” *Journal of machine learning research*, vol. 9, no. Nov, pp. 2579–2605, 2008.
- [55] H. G. Nasief, I. M. Rosado-Mendez, J. A. Zagzebski, and T. J. Hall, “Acoustic properties of breast fat,” *Journal of Ultrasound in Medicine*, vol. 34, no. 11, pp. 2007–2016, 2015.